Efficient method for analyzing magneto-oscillations of two-dimensional spin-orbit coupled electron gases

Hamed Gramizadeh [1], Denis R. Candido [2], Andrei Manolescu [1], J. Carlos Egues [3,4] and Sigurdur I. Erlingsson [1,*]

[1]*Department of Engineering, Reykjavik University, Menntavegi 1, IS-102 Reykjavik, Iceland*
[2]*Department of Physics and Astronomy, University of Iowa, Iowa City, Iowa 52242, USA*
[3]*Instituto de Física de São Carlos, Universidade de São Paulo, 13560-970 São Carlos, São Paulo, Brazil*
[4]*Department of Physics, University of Basel, CH-4056, Basel, Switzerland*

Magneto-oscillations in two-dimensional systems with spin-orbit interaction (SOI) are typically characterized by fast Shubnikov–de Haas (SdH) oscillations and slower spin-orbit-related beatings. The characterization of the full SdH oscillatory behavior in systems with both SOI and Zeeman coupling requires a time-consuming diagonalization of large matrices for many magnetic field values. By using the Poisson summation formula, we can explicitly separate the density of states into fast and slow oscillations, which determine the corresponding fast and slow parts of the magneto-oscillations. We introduce an efficient scheme of partial diagonalization of our Hamiltonian, where only states close to the Fermi energy are needed to obtain the SdH oscillations, thus reducing the required computational time. This allows an efficient method for numerically fitting the SdH data, using the inherent separation of the fast and slow oscillations. We compare systems with only Rashba SOI and both Rashba and Dresselhaus SOI with and without an in-plane magnetic field. The energy spectra are characterized in terms of symmetries, which have direct and visible consequences in the magneto-oscillations. To highlight the benefits of our methodology, we use it to extract the spin-orbit parameters by fitting realistic transport data.

I. INTRODUCTION

Two-dimensional (2D) electronic systems are believed to hold the promise of improved device characteristics [1,2]. In spintronics [3], spin-orbit interaction (SOI) plays an important role in many physical phenomena, e.g., the spin Hall effect [4–6] and the persistent spin helix [7–9]. In addition, it underlies the physical mechanisms for, e.g., 2D topological insulators and quantum spin Hall materials [10–12]. Nevertheless, extracting physical or model parameters associated with these systems is rarely straightforward, and often a challenging endeavor.

Shubnikov–de Haas (SdH) oscillations [13,14] have been an important tool to characterize charge densities and scattering times in 2D semiconductors [15]. In addition, the SdH oscillations have been used to extract the Rashba and Dresselhaus SOIs [16]. An earlier theoretical description showed that the SOI leads to changes in the oscillation beating pattern [17], and further analysis of the same group incorporated the known exact result [18] to improve the analysis of the Rashba and Zeeman coupling [19]. As is pointed out in Ref. [19], the study and interpretation of oscillations in the magnetoresistance relies on some assumptions, as for example, what the dominant source of SOI is. A method that has often been used to estimate the strength of the Rashba coupling was introduced in Refs. [20–22], which uses the density of states (DOS) at zero magnetic field to relate the DOS to the Rashba SOI strength α. However, this method has drawbacks since it cannot account

for Zeeman (via the g factor g^*) or Dresselhaus spin-orbit coupling strength β [23,24]. There have been some attempts to analyze the SdH oscillations in terms of α, β, and g^*, but they have mostly involved qualitative comparison with the energy spectrum of pure Rashba and pure Dresselhaus, resulting in nominally identical samples being characterized as either Rashba dominated [24] or Dresselhaus dominated [25]. In addition, the method used in Ref. [26] is based on the position of beating nodes, but for comparable strength of Rashba and Dresselhaus couplings, the beating nodes can vanish. Therefore, a systematic way of analyzing the experimental data in terms of oscillation envelope shape rather than beating node positions is required. This is what we present here.

Magnetoresistance oscillations were considered by Averkiev *et al.* [27] and Tarasenko and Averkiev [28] for the special case of $\alpha = \beta$ and no Zeeman coupling. They showed that the beatings vanished for this case since the corresponding spectrum consists of equally spaced Landau levels. Furthermore, the effects of Zeeman splitting and tilted magnetic field (in the absence of spin-orbit coupling) were considered in Ref. [29]. In Ref. [30], full numerical calculations of magneto-oscillations were performed for relatively high magnetic fields and low electron densities, which is far away from the regime of recent experimental works [31]. In Refs. [31,32], numerical calculations of magnetoresistivity oscillations were performed, but a general analysis of the oscillations, relating the frequency and position of the beating pattern directly to α and β, was not presented. Such connections are very important for experimental works, as they allow the extraction of system parameters. In a recent experimental work, SdH oscillations were considered in InAs 2D electron gases (2DEGs), where

*sie@ru.is

the Rashba SOI was tuned, but there were unresolved issues concerning the fitting of the cubic Dresselhaus coupling constant γ, resulting in $\gamma = 0$ [31]. Furthermore, the effects of the tilted magnetic field were theoretically considered in the context of the cyclotron and electric-dipole spin resonances in the presence of both Rashba and Dresselhaus SOIs [32]. For tilting angles at which the Zeeman splitting and cyclotron energy were equal, the effects of the SOI could be made more pronounced. This has been used in more recent experiments studying magnetization [26] and magneto-oscillations [33], although the analysis suffers from the same issues discussed in Ref. [24], i.e., being based on the $B = 0$ DOS and not accounting explicitly for nonzero g^* or β.

In this paper, we introduce an efficient method to obtain the relevant energy spectrum for magnetotransport, in the presence of both Rashba and Dresselhaus SOIs and Zeeman coupling. Our method is based on the diagonalization of a partial/truncated Hamiltonian and allows a faster calculation and clearer interpretation of SdH magneto-oscillations. In Sec. II, we introduce the system properties and the partial Hamiltonian. In Sec. III, we present the DOS using the Poisson summation formula and highlight the fast and slow oscillations. Finally, we apply our method to accurately fit realistic magneto-oscillation data, highlighting the speed and convenience of our method.

II. HAMILTONIAN AND NUMERICAL DIAGONALIZATION

Our focus will be on 2DEG in the presence of a magnetic field $\mathbf{B} = [B_\| \cos(\phi), B_\| \sin(\phi), B_\perp]$, where $B_\perp$ is the component of the magnetic field perpendicular to the 2DEG, and $B_\|$ is the corresponding in-plane component. In addition, we consider both Rashba [18] and Dresselhaus [23] spin-orbit couplings. The resulting Hamiltonian is

$$
H_{2D} = \frac{1}{2m^*}\left(\pi_x^2 + \pi_y^2\right) + \frac{g^*\mu_B}{2}B_\perp\sigma_z
$$
$$
+ \frac{g^*\mu_B B_\|}{2}[\sigma_x \cos(\phi) + \sin(\phi)\sigma_y]
$$
$$
+ \frac{\alpha}{\hbar}(\pi_y\sigma_x - \pi_x\sigma_y) + \frac{\beta}{\hbar}(\pi_x\sigma_x - \pi_y\sigma_y), \quad (1)
$$

where $\hbar$ is the reduced Planck's constant, m^* is the effective electron mass, g^* is the effective g factor, μ_B is the Bohr magneton, and σ_x, σ_y, and σ_z denote the usual Pauli matrices. The angle θ describes the tilting of the magnetic field away from the perpendicular direction. Throughout this paper we choose $B \equiv B_\perp$ to be fixed for all tilting angles, which is done to ease the comparison between different tilting angles, with the absolute value of the applied magnetic field $B/\cos(\theta)$. The strengths of the Rasbha and Dresselhaus SOIs are determined by the coefficients α and β, respectively. The momenta are given by $\pi_x = p_x - eBy/2$ and $\pi_y = p_y + eBx/2$, where $e > 0$ is the elementary electrical charge. Note that the gauge is chosen such that $B_\|$ drops out from the momenta once the three-dimensional (3D) problem is projected onto the lowest transverse level. Next, we introduce the ladder operators:

$$
a = \frac{\ell_c}{\sqrt{2}\hbar}(\pi_x - i\pi_y), \quad \text{and} \quad a^\dagger = \frac{\ell_c}{\sqrt{2}\hbar}(\pi_x + i\pi_y), \quad (2)
$$

where $\ell_c = \sqrt{\frac{\hbar}{eB}}$ is the magnetic length. The ladder operators obey the commutation relation $[a, a^\dagger] = 1$, as a consequence of the canonical commutation relations $[x, p_x] = i\hbar$ and $[y, p_y] = i\hbar$. The Hamiltonian then reduces to

$$
\frac{H_{2D}}{\hbar\omega_c} = a^\dagger a + \frac{1}{2} + \frac{\tilde{\Delta}}{2}\left[\sigma_z + \frac{\tan(\theta)}{2}(\sigma_+ e^{i\phi} + \sigma_- e^{-i\phi})\right]
$$
$$
+ \frac{\beta}{\sqrt{2}\hbar\omega_c\ell_c}(a^\dagger\sigma_+ + a\sigma_-)
$$
$$
- \frac{i\alpha}{\sqrt{2}\hbar\omega_c\ell_c}(a^\dagger\sigma_- - a\sigma_+), \quad (3)
$$

where the Zeeman term $\tilde{\Delta} = \frac{g^*\mu_B B}{\hbar\omega_c} = \frac{g^* m^*}{2m_0}$, with m_0 being the bare electron mass, inherited its sign from g^*, $\omega_c = eB/m^*$ is the cyclotron frequency, and $\sigma_\pm = \sigma_x \pm i\sigma_y$. Although we use a specific form in Eq. (3) corresponding to Rashba and (linear) Dresselhaus couplings, the numerical procedure presented here can be applied to general 2D Hamiltonians with nonzero perpendicular magnetic fields that contain ladder operators and Pauli matrices, e.g., topological insulators with linear dispersion [12] and cubic Dresselhaus SOIs [16]. The standard way of obtaining the spectrum of the Hamiltonian Eq. (3) is by creating a matrix of dimension $2N \times 2N$, where N is the number of eigenstates of $a^\dagger a$ (i.e., $a^\dagger a|m\rangle = m|m\rangle$, $m = 0, 1, \ldots, N - 1$), in addition to accounting for the spin-degree (i.e., $\sigma_z|\sigma\rangle = \sigma|\sigma\rangle$, $\sigma = \pm 1$). The choice of N depends on the number of eigenstates that are required for a given problem. In the case of magnetotransport calculations in semiconductor quantum wells with densities $\sim 10^{12}$ cm^{-2} [26,31], the required eigenstates are counted in the hundreds, and to calculate those states accurately, the size of N should be ~ 4 times larger [34], resulting in $N \sim 10^3$. Although diagonalizing a single such matrix does not represent a computational challenge, the diagonalization must be repeated for multiple values of magnetic field (measured in the thousands), and α, β, etc. Accounting for all this, calculating a set of magnetoresistance curves can lead to computational time around multiple hours [35].

The method we introduce here is designed to efficiently calculate the eigenenergies for a given n, which labels the Landau levels. Before outlining the methods, we first discuss general properties of the Hamiltonian in Eq. (3). If we have $\beta = \theta = 0$, we can obtain exact eigenvalues (see Appendix A):

$$
\varepsilon_{n,+} = n + 1 - \sqrt{\frac{(1 - \tilde{\Delta})^2}{4} + 4\frac{\varepsilon_R}{\hbar\omega_c}(n + 1)}, \quad (4)
$$

$$
\varepsilon_{n,-} = n + \sqrt{\frac{(1 - \tilde{\Delta})^2}{4} + 4\frac{\varepsilon_R}{\hbar\omega_c}n}, \quad (5)
$$

where $\varepsilon_R = \frac{m^*\alpha^2}{2\hbar^2}$. These eigenvalues are plotted in Fig. 1(a) for $n = 150$ (dashed orange curve). When the same system is diagonalized numerically, the energy spectra take a sawtooth shape since the numerical diagonalization orders the eigenvalues according to their size, and crossings turn into anticrossings (black dotted lines). There is an underlying parity symmetry for $\theta = 0$, introduced in Refs. [36,37] for $\alpha = \beta$ and later extended for systems with Rashba and Dresselhaus
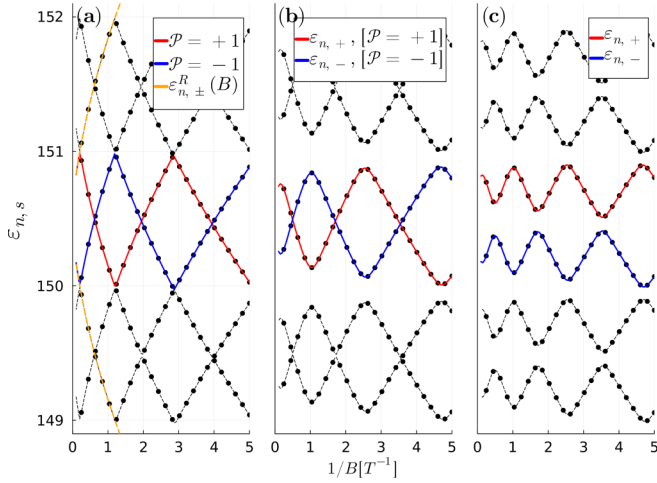
FIG. 1. Comparison of full diagonalization (black points) and partial Hamiltonian (red and blue curves), for (a) $\alpha = 7.5$ meV nm, $\beta = 0$, (b) $\alpha = 7.5$ meV nm, $\beta = 3.0$ meV nm, and (c) $\alpha = 7.5$ meV nm, $\beta = 3.0$ meV nm, $\theta = \pi/3$, and $\phi = 0$. Other parameters are $m^* = 0.04$, $g^* = -12$, and $n_{2D} = 0.0176$ nm^{-2} for InAs-based systems [31].

couplings in Ref. [38]. This parity allows the spectrum to be split into two separate subspaces that can be diagonalized separately, see Appendix B 1. When this is done, we obtain states with different parities crossing each other, as they belong to different parity subspaces (blue and red curves). However, they anticross with other states that belong to the same parity space.

In Fig. 1(b), a nonzero value of $\beta = 3.0$ meV nm is added, which opens overall gaps in the spectrum [39] but leaves some crossings unaffected, i.e., crossings of states that belong to different parity subspace (see Appendix B 1). The spectrum now consists of pairs of states for each value of n and $s = \pm 1$ which cross but anticross with adjacent states above and below. Finally, in Fig. 1(c), an in-plane component of the magnetic field is added with $\theta = \pi/3$ and $\phi = 0$. For this case, the parity is no longer a good quantum number, i.e., the parity operator does not commute with H_{2D}, and extra anticrossings open between $|n, +\rangle$ and $|n, -\rangle$ states corresponding to eigenenergies $\varepsilon_{n,+}$ and $\varepsilon_{n,+}$, respectively.

A. Numerical methods

Now we turn to describing the numerical diagonalization procedure. As can be seen in Figs. 1(b) and 1(c), the eigenstates are always pushed up or down by their couplings to adjacent states. This results in each state following a unique curve which can be tracked, as a function of $1/B$, for all n. Based on this, we introduce a partial diagonalization (PD) outlined in Fig. 2, where $n = 0, 1, 2 \ldots$ is the Landau level index of interest. The matrix representation of Eq. (3) can be written as a block-tridiagonal matrix with diagonal 2×2 blocks:

$$\frac{[H_{2D}]_{m,m}}{\hbar\omega_c} = \begin{bmatrix} m + \frac{1}{2} + \frac{\tilde{\Delta}}{2} & \frac{\tilde{\Delta}}{2}\tan(\theta)e^{i\phi} \\ \frac{\tilde{\Delta}}{2}\tan(\theta)e^{-i\phi} & m + \frac{1}{2} - \frac{\tilde{\Delta}}{2} \end{bmatrix}, \quad (6)$$
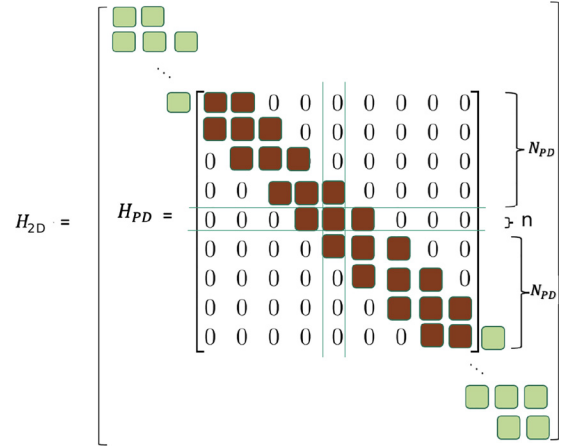

FIG. 2. The structure of H_{PD} illustrated relative to the full matrix H_{2D}. For a given value of n, the partial matrix H_{PD} is constructed around matrix element $[H_{2D}]_{n,n}$.

and the off-diagonal 2×2 block is given by

$$\frac{[H_{2D}]_{m,m+1}}{\hbar\omega_c} = \sqrt{m+1}\frac{1}{\sqrt{2}\hbar\omega_c\ell_c}\begin{bmatrix} 0 & 2\beta \\ -2i\alpha & 0 \end{bmatrix}. \quad (7)$$

With these, we construct the partial matrix H_{PD} centered on block n with N_{PD} blocks above and below. The resulting matrix has dimension $2(2N_{PD} + 1) \times 2(2N_{PD} + 1)$.

If the parity is a good quantum number, i.e., $\theta = 0$, then each block in H_{PD} is halved (i.e., becomes 1×1) when each parity subspace is considered, see Appendix B 1 for details. For states with $n \leqslant N_{PD}$, the lower part of the partial matrix is decreased accordingly, and for $n = 0$, only N_{NP} states above n are needed. With this, the entire spectrum can be calculated for each value of n. To test the accuracy of this procedure, we calculate the relative deviation between the full numerical diagonalization $\varepsilon_{n,s}^{[num]}$ for $N = 1000$ and the eigenstates obtained with the PD, $\varepsilon_{n,s}^{[PD]}$, at $B = 0.15$ T for $\alpha = 7.5$ meV nm, $\beta = 3.0$ meV nm, and $\theta = 0$. Figure 3 shows our results for $N_{PD} = 8, 12, 16$, and 20. The value $B = 0.15$ T corresponds to the typical lowest value of the magnetic field where magneto-oscillations become visible in experiments. This also corresponds to the case where the spin-orbit terms in Eq. (3) (proportional to $1/\sqrt{B}$) are relatively largest and most numerically challenging, and the value of N_{PD} is set in this regime. For higher magnetic fields, the Hamiltonian matrix becomes diagonally dominant and less numerically challenging. Already for $N_{PD} = 16$, the relevant eigenenergies (first quarter of eigenvalues) have a relative deviation $<10^{-10}$, and for $N_{PD} = 20$, the machine precision is reached for all relevant eigenvalues.

As we will see in the next section, allowing n to take noninteger values can be useful in calculating the DOS and transport properties. As is discussed in Appendix B 1, this can be implemented via the PD, i.e., one can calculate eigenenergies $\varepsilon_{n+\Delta x,s}$, where $\Delta x \in [-0.5, 0.5]$ is a real number. The interval is set by the condition that $\varepsilon_{n+\Delta x,s} = \varepsilon_{n+1-\Delta x,s}$, i.e., $\Delta x = 0.5$ corresponds to a crossing with the next state above, and similarly, $\Delta x = -0.5$ corresponds to a crossing with the next state below.
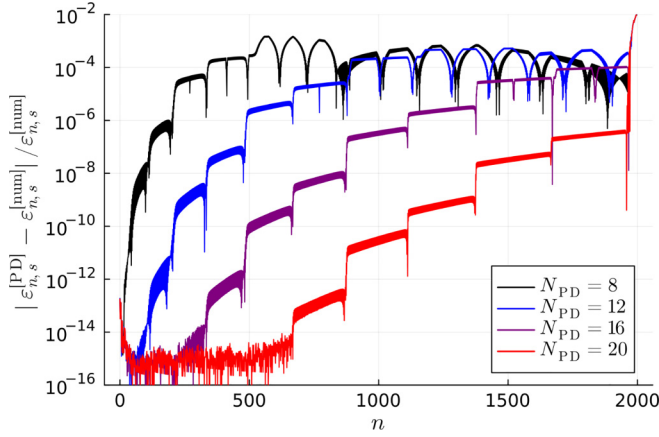
FIG. 3. Relative deviation between eigenstates obtained using full numerical diagonalization with $N = 1000$, $\varepsilon_{n,s}^{[\text{num}]}$, and the eigenstates with the partial diagonalization $\varepsilon_{n,s}^{[\text{PD}]}$ as a function of N_{PD} for magnetic field $B = 0.15$ T. Parameter values are $\alpha = 7.5$ meV nm, $\beta = 3.0$ meV nm, and $\theta = 0$. Other parameters are $m^* = 0.04$, $g^* = -12$, and $n_{2D} = 0.0176$ nm^{-2} for InAs-based systems [31].

III. DOS AND F FUNCTION

The eigenenergies of the Hamiltonian in Eq. (1) result in a discrete spectrum, the well-known Landau levels [15]. The resulting DOS is given by

$$D(E, B) = \frac{1}{2\pi \ell_c^2} \sum_{n=0}^{\infty} \sum_s L_\Gamma[E - \hbar\omega_c \varepsilon_{ns}(B)], \quad (8)$$

where $1/2\pi \ell_c^2$ accounts for the Landau level degeneracy (per spin), and $L_\Gamma(x)$ describes broadening due to impurity scattering [15]. Here, it is assumed that all levels are broadened by a phenomenological parameter Γ, e.g., $\delta(\cdot) \rightarrow L_\Gamma(\cdot)$, for Gaussian broadening with $L_\Gamma(x) = \exp(-\frac{x^2}{2\Gamma^2})/\sqrt{2\pi \Gamma^2}$. In addition, we assume that $E = E_F$, where $E_F = \hbar^2 \pi n_{2D}/m^*$ and n_{2D} is the 2D electron density. Our goal is to rewrite the DOS in a way that highlights the fast and slow oscillations, which are not directly evident in Eq. (8). This is achieved by using the Poisson summation formula [15,16,29,40], which results in

$$\delta D(B) \equiv \frac{D(E_F, B) - D_0}{D_0}$$

$$\simeq 2 \sum_{l=1}^{\infty} \tilde{L}\left(l\frac{\Gamma}{\hbar\omega_c}\right) \cos(l2\pi \mathcal{F}_+) \cos(l2\pi \mathcal{F}_-), \quad (9)$$

where $D_0 = \frac{\hbar^2}{\pi m^*}$ is the zero-field DOS, $\tilde{L}_\Gamma$ is the cosine transform of the broadening function, and the functions $\mathcal{F}_\pm = \frac{1}{2}(F_+ \pm F_-)$ represent the fast (+) and slow (−) parts of the SdH oscillations, respectively. Details of this derivation are found in Appendix C. The functions $F_s = F_s(E_F, B)$, with $s = \pm 1$, are defined by the relation

$$\varepsilon_{n,s}(B) = \frac{E_F}{\hbar\omega_c} \Leftrightarrow n = F_s(E_F, B), \quad (10)$$

so determining F_s numerically becomes a root finding problem. If $\varepsilon_{n,s}(B)$ is a continuous and differentiable function of n, then one can always find $n = F_n(E_F, B)$, i.e., the noninteger
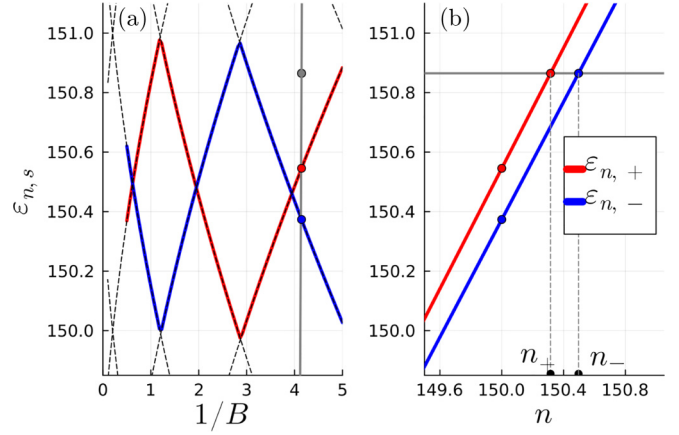

FIG. 4. (a) Energy level $n = 150$ using the partial diagonalization (PD) algorithm, along with adjacent states (dashed black line) for $\alpha = 7.5$ meV nm and $\beta = 0.0$. The solid gray line shows $E_F/\hbar\omega_c$, and its value at $1/B = 4.145$ (gray circle). (b) The energy levels $\varepsilon_{n,s}(B)$ as a function of n showing the intersection with $E_F/\hbar\omega_c$ at $1/B = 4.145$. Other parameters are $m^* = 0.04$, $g^* = -12$, and $n_{2D} = 0.0176$ nm^{-2} for InAs-based systems [31].

value of n that fulfills $\varepsilon_{n,s}(B) = E_F/\hbar\omega_c$ [40]. In Fig. 4(a), we plot a zoom-in of $\varepsilon_{n,s}(B)$ along with $E_F/\hbar\omega_c$ (gray solid line). Accepting noninteger values of n allows the energy levels to cross $E_F/\hbar\omega_c$ for fixed values of $1/B$ and E_F. The dominant behavior of $\varepsilon_{n,s}(B)$ with respect to n is linear (see Appendix A), as is visible in Fig. 4(b). The energy levels cross $E_F/\hbar\omega_c$ at values n_+ and n_-, for $\varepsilon_{n,+}(B)$ and $\varepsilon_{n,-}(B)$, respectively, which are the values of the corresponding F_s functions: $n_s = F_s(E_F, B)$.

As seen in Fig. 1(b), gaps open in the spectrum when both α and β are nonzero. In Fig. 5(a), a zoom-in of $\varepsilon_{n,s}(B)$ is shown along with $E_F/\hbar\omega_c$ (gray solid line) for
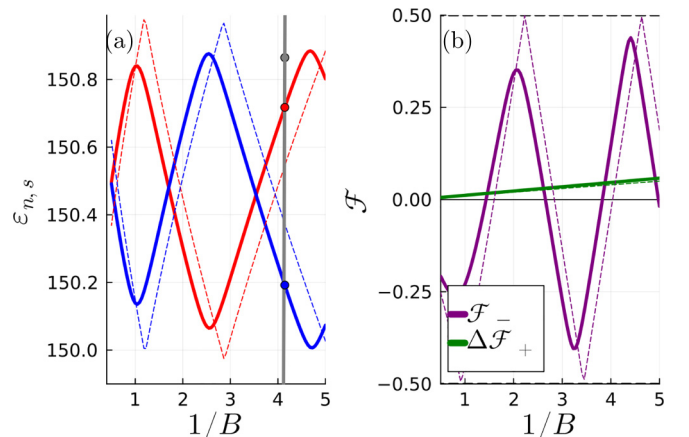

FIG. 5. (a) Energy level $n = 150$ using the partial diagonalization (PD) algorithm for $\alpha = 7.5$ meV nm and $\beta = 3.0$ meV nm. The dashed curves correspond to $\alpha = 7.5$ meV nm and $\beta = 0$. The solid gray line shows $E_F/\hbar\omega_c$, and its value at $1/B = 4.145$ (gray circle). (b) The $\mathcal{F}$ function for $\alpha = 7.5$ meV nm and $\beta = 3.0$ meV nm (solid lines), and pure Rashba, $\beta = 0$ (dashed line). Other parameters are $m^* = 0.04$, $g^* = -12$, and $n_{2D} = 0.0176$ nm^{-2} for InAs-based systems [31].
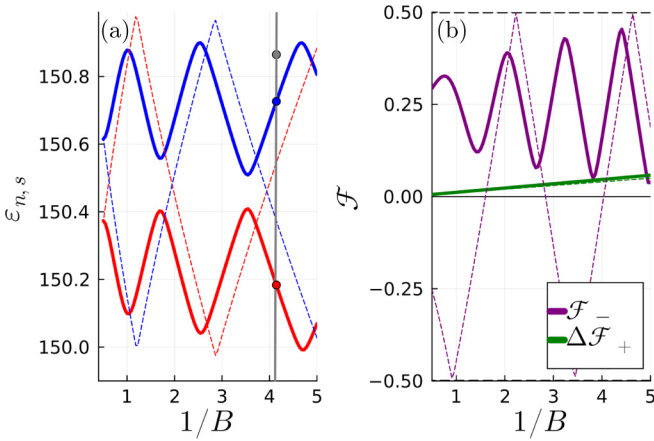
FIG. 6. (a) Energy level $n = 150$ using the partial diagonalization (PD) algorithm for $\alpha = 7.5$ meV nm, $\beta = 3.0$ meV nm, $\theta = \pi/3$, and $\phi = 0$. The dashed curves correspond to $\alpha = 7.5$ meV nm and $\beta = 0$. The solid gray line shows $E_F/\hbar\omega_c$ and its value at $1/B = 4.145$ (gray circle). (b) The $\mathcal{F}$ function for $\alpha = 7.5$ meV nm and $\beta = 3.0$ meV nm (solid lines), and pure Rashba, $\beta = 0$ (dashed line). Other parameters are $m^* = 0.04$, $g^* = -12$, and $n_{2D} = 0.0176$ nm^{-2} for InAs-based systems [31].

$\alpha = 7.5$ meV nm and $\beta = 3.0$ meV nm. The dashed curves are the corresponding pure Rashba eigenenergies. Note the sawtooth shape of the dashed curves since all states cross in this case. The corresponding $\mathcal{F}$ functions are shown in Fig. 5(b). The anticrossings in the spectrum are visible as a rounding of the sawtooth shape, and level crossings correspond to $\mathcal{F}_- = 0$.

It is instructive to look at the $\mathcal{F}_\pm$ function in the case of pure Rashba SOI:

$$\mathcal{F}_+ = \frac{E_F}{\hbar\omega_c} + \frac{2\varepsilon_R}{\hbar\omega_c} - \frac{1}{2} = \frac{h}{2e}n_{2D}\frac{1}{B} - \frac{1}{2} + \frac{2\varepsilon_R}{\hbar\omega_c}, \quad (11)$$

$$\mathcal{F}_- = -\frac{1}{2} + \sqrt{\frac{(1-\tilde{\Delta})^2}{4} + \frac{\varepsilon_R E_F}{(\hbar\omega_c)^2}} \approx \frac{m^*\alpha k_F}{e\hbar}\frac{1}{B}, \quad (12)$$

where $k_F = \sqrt{2\pi n_{2D}}$, and the approximate sign in Eq. (12) refers to the low field limit. Since the SdH oscillation frequency in Eq. (11) is dominated by the term proportional to n_{2D}, we define the spin-orbit-related contribution to the fast oscillations as

$$\Delta\mathcal{F}_+ \equiv \mathcal{F}_+ - \left(\frac{h}{2e}n_{2D}\frac{1}{B} - \frac{1}{2}\right). \quad (13)$$

This allows us to plot on the same graph the slow spin-orbit-related oscillations described by $\mathcal{F}_-$ and the spin-orbit-related modification of the fast oscillation $\Delta\mathcal{F}_+$. Note that the sawtooth shape in Fig. 5(b) for the case of pure Rashba SOI (purple dashed curve) has a fixed slope $\pm\frac{m^*\alpha k_F}{e\hbar}$. This is equivalent to the result in Eq. (12), which is linear in $1/B$, since $\cos(2l\pi\mathcal{F}_-) = \cos(-2l\pi\mathcal{F}_-)$, i.e., the sign of the $\mathcal{F}_-$ slope is irrelevant. Finally, we consider the influence of an in-plane component of the magnetic field, i.e., $\theta \neq 0$. In this case, the parity symmetry no longer holds, and all states anticross, as seen in Fig. 6(a). This results in no states simultaneously crossing E_F, due to the level repulsion. Note that $\mathcal{F}_- = 0$ corresponds to both pseudospin species simultane-

ously crossing E_F at a given B field. These new anticrossings have a direct effect on the $\mathcal{F}_-$ function here, which never reaches zero, as opposed to Fig. 5(b), where $\mathcal{F}_-$ takes both positive and negative values. The $\mathcal{F}_-$ thus contains information on how close to (or far from) each other states with opposite s cross E_F. This property is useful when interpreting so-called *coincidence measurements* [41] that have been used to map out level crossings in SdH oscillations in 2DEGs in tilted magnetic fields [42,43].

IV. FITTING MAGNETOTRANSPORT DATA

The oscillation frequencies introduced in the previous section allow for a convenient separation of tasks when analyzing the magneto-oscillations. In 2D systems, the longitudinal resistance is proportional to the DOS [15], so the previous analysis applies directly to their magneto-oscillations. The rapid oscillations, i.e., SdH oscillation frequency $f^{SdH} = \frac{h}{2e}n_{2D}$, can be easily extracted by calculating the frequency spectrum via fast Fourier transform, thus yielding the 2DEG density n_{2D} [21,31]. The remaining parameters (α, β, and Γ) can be found by fitting the slow spin-orbit-related oscillations. We outline below this procedure for fitting realistic magnetoresistance data.

Our starting point is Eq. (8), which we use to generate realistic magnetoresistance data like the experimental data in Fig. S4 in Ref. [31]. We use parameters $\Gamma = 0.45$ meV, $n_{2D} = 0.019$ nm^{-2} (corresponding to $E_F = 114$ meV), $\alpha = 7.20$ meV nm, and $\beta = 2.40$ meV nm, and add a slight background and noise components to better mimic realistic data. The resulting $R_{xx}(B)$ is shown in Fig. 7(a), where a slight upward slope is barely discernible. From the R_{xx} data, the normalized magneto-oscillation is calculated:

$$\Delta R_{xx} = \frac{R_{xx}(B) - R_{xx;0}}{R_{xx;0}}, \quad (14)$$

where $R_{xx;0}$ is defined as the resistance at the magnetic field where the oscillations have been fully suppressed, in this case, for $B \leqslant 0.25$ T. This is plotted in Fig. 7(b), where the extrema have been marked with black dots, and central points (zeros) are marked with red dots. The background signal showing a slight upward trend is now more visible. The data are brought to the proper normalized magneto-oscillation form, shown in Fig. 7(c), by subtracting the background using a simple linear interpolation between the middle points [red points in Fig. 7(b)]. At this point, the data can be directly fitted to the slow oscillating terms in Eq. (9) using only a small number of points (black dots). Due to background compensation, we introduce an extra parameter R_0, so the resulting slow envelope function used for fitting is [38,44]

$$\delta\rho_{xx}(B) = 4R_0\tilde{L}_\Gamma\left(\frac{\Gamma}{\hbar\omega_c}\right)\cos[2\pi\mathcal{F}_-(B;\alpha,\beta)]. \quad (15)$$

Fitting the data in Fig. 7(c) to Eq. (15) results in a slow envelope shown in Fig. 8(a). The results of the fitting yield parameter values $R_0 = 0.65 \pm 0.07$, $B_q = 0.71 \pm 0.03$ T, $\alpha = (7.24 \pm 0.06)$ meV nm, and $\beta = (2.5 \pm 0.3)$ meV nm. The fitting only takes a few tens of seconds and a few attempts
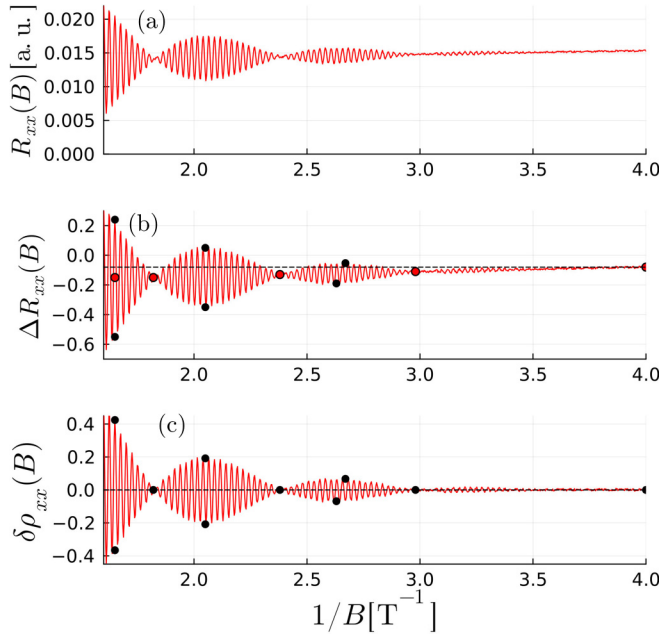
FIG. 7. (a) Magnetoresistance data generated using Eq. (8) with $\Gamma = 0.45$ meV, $n_{2D} = 0.019$ nm^{-2}, $\alpha = 7.20$ meV nm, and $\beta = 2.40$ meV nm. Slight background slope and random noise is to mimic realistic measurements. (b) Normalized magneto-oscillations showing slope due to background. Extrema and zeros are indicated by black and red dots, respectively. (c) Proper normalized magneto-oscillations after subtracting background (see Sec. IV for details). Other parameters are $m^* = 0.04$, $g^* = -12$ [31].
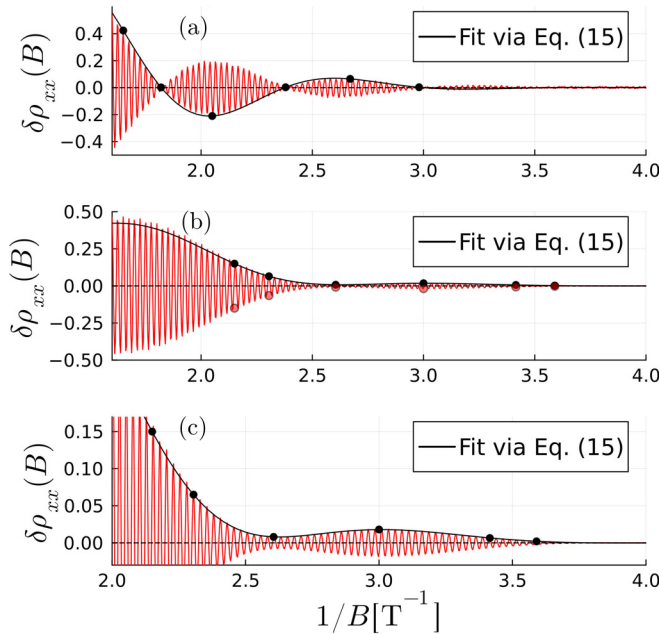

FIG. 8. (a) The normalized magneto-oscillations along with fitted curve through six data points (black dots). Resulting fitted parameters are $\alpha = (7.24 \pm 0.06)$ meV nm and $\beta = (2.5 \pm 0.3)$ meV nm. (b) Normalized magneto-oscillations generated using Eq. (8) with $\Gamma = 0.45$ meV, $\alpha = 3.30$ meV nm, and $\beta = 5.60$ meV nm (see main text). (c) Zoom-in on reference points and fitted curve which yields fit values $\alpha = (3.33 \pm 0.03)$ meV nm and $\beta = (5.63 \pm 0.02)$ meV nm.

for finding a good starting point for the fitting parameters. Note that the time to generate the full data took a couple of hours (on the same computer). Attempting to fit real transport data using Eq. (8), which requires calculating the whole spectrum $\varepsilon_{n,s}(B)$ for all B values to capture both fast and slow oscillations, would thus be prohibitively time consuming. Our method circumvents this problem by extracting the important slow spin-orbit-related oscillations via $\mathcal{F}_-(B)$, which are easily fitted using only 5–10 magnetic field points.

Finally, we point out that, for cases where Rashba and Dresselhaus SOI parameters are close to each other in value, the slow part of the magneto-oscillations does not cross zero, i.e., there are no beating nodes [38]. This can be seen in magneto-oscillation data in Fig. 8(b) generated using $\alpha = 3.30$ meV nm and $\beta = 5.60$ meV nm. The background can be subtracted using center points between the red and black dots. In Fig. 8(c), a zoom-in of the reference points and fitted curve is shown. The fit values are $\alpha = (3.33 \pm 0.03)$ meV nm and $\beta = (5.63 \pm 0.02)$ meV nm, which are in very good agreement with the parameter values used to generate the original data. Note that, in both cases of Figs. 8(a) and 8(b), the reference points fulfill $\delta\rho_{xx} < 0.4$, which ensures that the higher harmonics can be neglected, due to the exponential suppression [38].

V. CONCLUSIONS

In this paper, we presented a method to efficiently calculate the relevant energy spectrum for SdH magneto-oscillation analysis. We showed that the numerical procedure along with the Poisson summation formula allow for an efficient calculation and a better understanding of the fast and slow magneto-oscillations. The spin-orbit parameters α and β and the Landau level broadening Γ can be uniquely extracted from $\mathcal{F}_-$, which oscillates slowly. To illustrate our method, we applied it to realistic magnetotransport data and found that fitting the slow oscillations yielded very quick and accurate fit results. The slow oscillations in $\mathcal{F}_-$ can also shed light on so-called coincidence measurements on tilted magnetic fields. Our method does not rely on finding beating nodes, so it can be used to fit data in cases of α and β being comparable in size.

APPENDIX A: $\varepsilon_{n,s}$ AND F_s IN THE CASE OF PURE RASHBA

The Hamiltonian in Eq. (3) with $\beta = \theta = 0$ results in the pure Rashba Hamiltonian:

$$\frac{H_R}{\hbar\omega_c} = \left(a^\dagger a + \frac{1}{2}\right) + \frac{\tilde{\Delta}}{2}\sigma_z + \frac{\alpha}{\sqrt{2}\hbar\omega_c \ell_c}(a^\dagger \sigma_- + a\sigma_-).$$

(A1)

This can be written in 2×2 subspaces $\{|n, \uparrow\rangle, |n+1, \downarrow\rangle\}$, $n = 0, 1, \ldots$, [38], which results in the matrix:

$$
\frac{H_{R;2\times2}}{\hbar\omega_c} = \begin{bmatrix} n + \frac{(1+\tilde{\Delta})}{2} & \frac{2\alpha}{\sqrt{2}\hbar\omega_c\ell_c}(n+1) \\ \frac{2\alpha}{\sqrt{2}\hbar\omega_c\ell_c}(n+1) & n+1 + \frac{(1-\tilde{\Delta})}{2} \end{bmatrix}
$$

$$
= (n+1) + \begin{bmatrix} \frac{(1-\tilde{\Delta})}{2} & \frac{\sqrt{2}\alpha}{\hbar\omega_c\ell_c}(n+1) \\ \frac{\sqrt{2}\alpha}{\hbar\omega_c\ell_c}(n+1) & -\frac{(1-\tilde{\Delta})}{2} \end{bmatrix}, \quad \text{(A2)}
$$

with eigenvalues:

$$
\varepsilon_{n,+} = (n+1) - \sqrt{\frac{(1-\tilde{\Delta})^2}{4} + \frac{2m^*\alpha^2}{\hbar\omega_c\hbar^2}(n+1)} \quad \text{(A3)}
$$

$$
\varepsilon_{n+1,-} = (n+1) + \sqrt{\frac{(1-\tilde{\Delta})^2}{4} + \frac{2m^*\alpha^2}{\hbar\omega_c\hbar^2}(n+1)}. \quad \text{(A4)}
$$

The above equations reduce to Eqs. (4) and (5) using $\varepsilon_R = \frac{m^*\alpha}{2\hbar^2}$. The labeling of the eigenstates is chosen such that, in the limit $\alpha \to 0$, the eigenstates evolve into the correct eigenstates in the absence of SOI: $\varepsilon_{n,+} \to \varepsilon_{n,\uparrow}^0$ and $\varepsilon_{n+1,-} \to \varepsilon_{n+1,\downarrow}^0$.

The definition of the DOS in Eq. (8) contains a sum over $n = 0, 1, 2, \ldots$ which can formally be written as an integral over the continuous variable x via the Poisson summation formula (also known as a trace formula [40]) in Eq. (C1). Since the eigenenergies $\varepsilon_{n,s}$ are a well-defined function of n, the index n can be replaced by a continuous variable $x \in [0, \infty)$. The derivative of the eigenenergies with respect to x can then be calculated:

$$
\frac{\partial \varepsilon_{x,+}}{\partial x} = 1 - \frac{\frac{2\varepsilon_R}{\hbar\omega_c}}{\sqrt{\frac{(1-\tilde{\Delta})^2}{4} + \frac{4\varepsilon_R}{\hbar\omega_c}(x+1)}}, \quad \text{(A5)}
$$

$$
\approx 1 - \sqrt{\frac{\varepsilon_R}{E_F}} \approx 1, \quad \text{(A6)}
$$

where we used $x + 1 \approx \frac{E_F}{\hbar\omega_c}$. The same argument applies to $\varepsilon_{x,-}$, i.e., $\frac{\partial \varepsilon_{x,-}}{\partial x} \approx 1$. In the case of nonzero β and/or θ, Eq. (3) will lead to anticrossings, which tend to flatten the square root behavior of the energy levels, see Figs. 1(b) and 1(c), thus making the approximation in Eq. (A6) even better.

APPENDIX B: PARTIAL HAMILTONIANS AND PARITY

Here, we describe the form of the partial Hamiltonian in the case of parity symmetry [38] and in the absence of that symmetry.

1. Matrix elements and parity symmetry

As was outlined in Ref. [38], the full basis $|m, \sigma\rangle$ can be split in two according to the eigenvalues of the parity operator:

$$
\hat{\mathcal{P}} = \exp\left\{i\pi\left[a^\dagger a + \frac{1}{2}(\sigma_z - 1)\right]\right\}, \quad \text{(B1)}
$$

which are $\mathcal{P} = \pm 1$. The basis states of the resulting parity subspace are then

$$
\mathcal{P} = +1: \quad \{|0, \uparrow\rangle, |1, \downarrow\rangle, |2, \uparrow\rangle, |3, \downarrow\rangle, |4, \uparrow\rangle, \ldots\}, \quad \text{(B2)}
$$

$$
\mathcal{P} = -1: \quad \{|0, \downarrow\rangle, |1, \uparrow\rangle, |2, \downarrow\rangle, |3, \uparrow\rangle, |4, \downarrow\rangle, \ldots\}. \quad \text{(B3)}
$$

The Hamiltonian matrix for each $\mathcal{P} = \pm 1$ subspace becomes a tridiagonal matrix with diagonal elements:

$$
[H_{2D}^{(+1)}]_{k,k} = k + \frac{1}{2} + \frac{\tilde{\Delta}}{2}(-1)^k, \quad \text{(B4)}
$$

$$
[H_{2D}^{(-1)}]_{k,k} = k + \frac{1}{2} - \frac{\tilde{\Delta}}{2}(-1)^k, \quad \text{(B5)}
$$

where $k = 0, 1, 2, \ldots$ labels the basis states in subspace $\mathcal{P} = \pm 1$. The alternating sign of the Zeeman term reflects the alternating $\uparrow$ and $\downarrow$ in the basis states in Eqs. (B2) and (B3). The off-diagonal matrix elements are given by

$$
[H_{2D}^{(+1)}]_{k,k+1} = \sqrt{k+1}\left\{\frac{i\alpha}{\sqrt{2}\hbar\omega_c\ell_c}[1 + (-1)^k]\right.
$$

$$
\left. + \frac{\beta}{\sqrt{2}\hbar\omega_c\ell_c}[1 - (-1)^k]\right\}, \quad \text{(B6)}
$$

$$
[H_{2D}^{(-1)}]_{k,k+1} = \sqrt{k+1}\left\{\frac{i\alpha}{\sqrt{2}\hbar\omega_c\ell_c}[1 - (-1)^k]\right.
$$

$$
\left. + \frac{\beta}{\sqrt{2}\hbar\omega_c\ell_c}[1 + (-1)^k]\right\}. \quad \text{(B7)}
$$

The $[1 \pm (-1)^k]$ terms take alternating values 0 and 2, which results in $[H_{2D}^{(+1)}]_{k,k+1} \propto \alpha$ for even values of k but, for odd k, gives $[H_{2D}^{(+1)}]_{k,k+1} \propto \beta$. For the $\mathcal{P} = -1$ parity subspace, the matrix elements in Eq. (B7), the even/odd pattern for k is switched. Compare this with Eq. (7) in the absence of parity symmetry, where each 2×2 block contains both α and β.

The partial Hamiltonian for $\mathcal{P} = +1$ centered on the nth Landau level is constructed from Eqs. (B4) and (B6):

$$
[H_{PD}^{(+1)}(n)]_{m,m} = \left[n + (m - N_{PD} - 1) + \frac{1}{2}\right]
$$

$$
+ \frac{\tilde{\Delta}}{2}(-1)^{(\bar{n}+m-N_{PD}-1)}, \quad \text{(B8)}
$$

$$
[H_{PD}^{(+1)}(n)]_{m,m+1} = \sqrt{(n + m - N_{PD} - 1) + 1}
$$

$$
\times \left\{\frac{i\alpha}{\sqrt{2}\hbar\omega_c\ell_c}[1 + (-1)^{(\bar{n}+m-N_{PD}-1)}]\right.
$$

$$
\left. + \frac{\beta}{\sqrt{2}\hbar\omega_c\ell_c}[1 - (-1)^{(\bar{n}+m-N_{PD}-1)}]\right\}, \quad \text{(B9)}
$$

where $\bar{n} = \text{round}(n)$ and $m \in [1, 2N_{PD} + 1]$. The eigenenergy $\varepsilon_{n,s}^{(+1)}$ is obtained as the $(N_{PD} + 1)$th eigenvalue of $H_{PD}^{(+1)}(n)$. In a similar fashion, the partial Hamiltonian for $\mathcal{P} = -1$,

centered on the nth Landau level, is given by

$$\left[H_{\text{PD}}^{(-1)}(n)\right]_{m,m} = \left[n + (m - N_{\text{PD}} - 1) + \frac{1}{2}\right]$$
$$+ \frac{\tilde{\Delta}}{2}(-1)^{(\bar{n}+m-N_{\text{PD}}-1)}, \quad \text{(B10)}$$

$$\left[H_{\text{PD}}^{(-1)}(n)\right]_{m,m+1} = \sqrt{(n + m - N_{\text{PD}} - 1) + 1}$$
$$\times \left\{\frac{i\alpha}{\sqrt{2}\hbar\omega_c\ell_c}[1 - (-1)^{(\bar{n}+m-N_{\text{PD}}-1)}]\right.$$
$$\left. + \frac{\beta}{\sqrt{2}\hbar\omega_c\ell_c}[1 + (-1)^{(\bar{n}+m-N_{\text{PD}}-1)}]\right\},$$
$$\text{(B11)}$$

and the eigenenergy $\varepsilon_{n,s}^{(-1)}$ is obtained as the $(N_{\text{PD}} + 1)$th eigenvalue of $H_{\text{PD}}^{(-1)}(n)$.

2. Matrix elements without parity symmetry

In the absence of parity symmetry, i.e., for $\theta \neq 0$, the matrix elements in Eqs. (6) and (7) are used to construct the partial matrix centered on the nth Landau level:

$$[H_{\text{PD}}(n)]_{m,m} = \left[(n + m - N_{\text{PD}} - 1) + \frac{1}{2}\right]\begin{bmatrix} 1 & 0 \\ 0 & 1 \end{bmatrix}$$
$$+ \begin{bmatrix} \frac{\tilde{\Delta}}{2} & \frac{\tilde{\Delta}}{2}\tan(\theta)e^{i\phi} \\ \frac{\tilde{\Delta}}{2}\tan(\theta)e^{-i\phi} & -\frac{\tilde{\Delta}}{2} \end{bmatrix}, \quad \text{(B12)}$$

$$[H_{\text{PD}}(n)]_{m,m+1} = \sqrt{(n + m - N_{\text{PD}} - 1) + 1}\frac{1}{\sqrt{2}\hbar\omega_c\ell_c}$$
$$\times \begin{bmatrix} 0 & 2\beta \\ -2i\alpha & 0 \end{bmatrix}, \quad \text{(B13)}$$

where $m \in [1, 2N_{\text{PD}} + 1]$. The eigenenergy pair $\varepsilon_{n,+}$ and $\varepsilon_{n,-}$ is obtained as eigenvalues of $H_{\text{PD}}(n)$ number $(2N_{\text{PD}} + 1)$ and $(2N_{\text{PD}} + 2)$.

APPENDIX C: POISSON'S SUMMATION FORMULA

Here, we will apply the Poisson summation formula:

$$\sum_{n=0}^{\infty} f(n) = \int_0^{\infty} dx f(x) + 2\sum_{l=1}^{\infty}\int_0^{\infty} dx f(x)\cos(l2\pi x),$$
$$\text{(C1)}$$

to the sum over the broadened Landau levels in Eq. (8). Starting with one spin species s:

$$\sum_{n=0}^{\infty} L_{\Gamma}[E_F - \hbar\omega_c\varepsilon_{n,s}(B)]$$
$$= \int_0^{\infty} dx L_{\Gamma}[E_F - \hbar\omega_c\varepsilon_{x,s}(B)]$$
$$+ \sum_{l=1}^{\infty}\int_0^{\infty} dx L_{\Gamma}[E_F - \hbar\omega_c\varepsilon_{x,s}(B)]\cos(l2\pi x). \quad \text{(C2)}$$

Next, we introduce a change of variables:

$$u = E_F - \hbar\omega_c\varepsilon_{x,s}(B), \quad \text{(C3)}$$

$$\frac{du}{dx} = -\hbar\omega_c\frac{\partial\varepsilon_{x,s}}{\partial x}. \quad \text{(C4)}$$

The derivative $\frac{\partial\varepsilon_{x,s}}{\partial x} = 1 + O(\sqrt{\varepsilon_R/E_F})$ when evaluated at $\varepsilon_{x,s} \approx E_F/\hbar\omega_c$:

$$\sum_{n=0}^{\infty} L_{\Gamma}[E_F - \hbar\omega_c\varepsilon_{n,s}(B)]$$
$$= \frac{1}{\hbar\omega_c}\left\{\int_{-\infty}^{\infty} du L_{\Gamma}(u) + 2\sum_{l=1}^{\infty}\int_{-\infty}^{\infty} du L_{\Gamma}(u)\right.$$
$$\left. \times \cos[l2\pi F_s(E_F - u, B)]\right\}. \quad \text{(C5)}$$

To keep the equations as concise as possible, we will now drop the B argument in both F_s and $\varepsilon_{x,s}$. The integrand in Eq. (C5) has width $\sim\Gamma$, and since $E_F \gg \Gamma$, we can use first-order Taylor expansion of the F_s function in terms of u:

$$F_s(E_F - u) = F_s(E_F) - F'(E_F)u + O(u^2)$$
$$\approx F_s(E_F) - \frac{1}{\hbar\omega_c}u, \quad \text{(C6)}$$

where we have used $\frac{dF_s(E_F)}{dE_F} = \frac{1}{\hbar\omega_c}$, which is a consequence of $\frac{\partial\varepsilon_{n,s}}{\partial n} = 1$. This can be shown using that $n = F_s(E_F)$ is the inverse function of $E_F = \hbar\omega_c\varepsilon_{n,s}$, i.e., $n = F_s(\hbar\omega_c\varepsilon_{n,s})$. Taking the derivative of this relation with respect to n results in

$$1 = \frac{dF_s(E_F)}{dE_F}\hbar\omega_c\frac{\partial\varepsilon_{n,s}}{\partial n} \approx \frac{dF_s(E_F)}{dE_F}\hbar\omega_c, \quad \text{(C7)}$$

which yields the relation below Eq. (C6). We can thus write Eq. (C5) as

$$\sum_{n=0}^{\infty} L_{\Gamma}(E_F - \hbar\omega_c\varepsilon_{n,s})$$
$$= \frac{1}{\hbar\omega_c}\left\{\int_{-\infty}^{\infty} du L_{\Gamma}(u) + 2\sum_{l=1}^{\infty}\cos[l2\pi F_s(E_F)]\right.$$
$$\left. \times \int_{-\infty}^{\infty} du L_{\Gamma}(u)\cos\left(l2\pi\frac{u}{\hbar\omega_c}\right)\right\}$$
$$= \frac{1}{\hbar\omega_c}\left\{1 + 2\sum_{l=1}^{\infty}\cos[l2\pi F_s(E_F, B)]\tilde{L}_{\Gamma}\left(l\frac{\Gamma}{\hbar\omega_c}\right)\right\},$$
$$\text{(C8)}$$

where the symmetric broadening will make the sine term appearing in the Taylor expansion vanish. The cosine transform is defined as

$$\tilde{L}_{\Gamma}\left(l\frac{\Gamma}{\hbar\omega_c}\right) = \int_{-\infty}^{\infty} du L_{\Gamma}(u)\cos\left(l2\pi\frac{u}{\hbar\omega_c}\right), \quad \text{(C9)}$$

which for Gaussian broadening, leads to

$$\tilde{L}_\Gamma\left(l\frac{\Gamma}{\hbar\omega_c}\right) = \exp\left(-\left[\sqrt{2}\pi\, l\,\frac{\Gamma}{\hbar\omega_c}\right]^2\right) = \exp\left(-l^2\frac{B_q^2}{B^2}\right),$$
(C10)

where $B_q = \sqrt{2}\pi\frac{m^*\Gamma}{\hbar e}$. Finally, applying this to Eq. (8) and using the trigonometric relation:

$$\cos(l2\pi F_+) + \cos(l2\pi F_+)$$
$$= 2\cos\left(l2\pi\frac{F_+ + F_-}{2}\right)\cos\left(l2\pi\frac{F_+ - F_-}{2}\right),\quad \text{(C11)}$$

and $\frac{1}{2\pi\ell_c^2}\frac{1}{\hbar\omega_c} = \frac{\hbar^2}{2\pi m^*}$ results in Eq. (9).

[1] X. Huang, C. Liu, and P. Zhou, npj 2D Mater. Appl. **6**, 51 (2022).

[2] P. Kaushal and G. Khanna, Mater. Sci. Semicond. Process. **143**, 106546 (2022).

[3] A. Hirohata, K. Yamada, Y. Nakatani, I.-L. Prejbeanu, B. Diény, P. Pirro, and B. Hillebrands, J. Magn. Magn. Mater. **509**, 166711 (2020).

[4] M. I. D'Yakonov and V. I. Perel, Sov. J. Expt. Theor. Phys. Lett. **13**, 467 (1971).

[5] M. I. Dyakonov and V. I. Perel, Phys. Lett. A **35**, 459 (1971).

[6] J. E. Hirsch, Phys. Rev. Lett. **83**, 1834 (1999).

[7] J. Schliemann, J. C. Egues, and D. Loss, Phys. Rev. Lett. **90**, 146801 (2003).

[8] B. A. Bernevig, J. Orenstein, and S.-C. Zhang, Phys. Rev. Lett. **97**, 236601 (2006).

[9] J. Fu, P. H. Penteado, M. O. Hachiya, D. Loss, and J. C. Egues, Phys. Rev. Lett. **117**, 226401 (2016).

[10] C. L. Kane and E. J. Mele, Phys. Rev. Lett. **95**, 226801 (2005).

[11] B. A. Bernevig and S.-C. Zhang, Phys. Rev. Lett. **96**, 106802 (2006).

[12] B. A. Bernevig, T. L. Hughes, and S.-C. Zhang, Science **314**, 1757 (2006).

[13] L. Shubnikov and W. J. de Haas, Commun. Phys. Lab. Univ. Leiden 207a, 207c, 207d, 210a (1930).

[14] L. Schubnikow and W. J. De Haas, Proceedings of the Royal Netherlands Academy of Arts and Science **33**, 363 (1930).

[15] T. Ihn, *Semiconductor Nanostructures* (Oxford University Press, New York, 2010).

[16] R. Winkler, *Spin-Orbit Coupling Effects in Two-Dimensional Electron and Hole Systems* (Springer Verlag, New York, 2003).

[17] B. Das, D. C. Miller, S. Datta, R. Reifenberger, W. P. Hong, P. K. Bhattacharya, J. Singh, and M. Jaffe, Phys. Rev. B **39**, 1411(R) (1989).

[18] Y. A. Bychkov and E. I. Rashba, J. Phys. C **17**, 6039 (1984).

[19] B. Das, S. Datta, and R. Reifenberger, Phys. Rev. B **41**, 8278 (1990).

[20] J. Nitta, T. Akazaki, H. Takayanagi, and T. Enoki, Phys. Rev. Lett. **78**, 1335 (1997).

[21] G. Engels, J. Lange, T. Schäpers, and H. Lüth, Phys. Rev. B **55**, R1958 (1997).

[22] T. Schäpers, G. Engels, J. Lange, T. Klocke, M. Hollfelder, and H. Lüth, J. Appl. Phys. **83**, 4324 (1998).

[23] G. Dresselhaus, Phys. Rev. **100**, 580 (1955).

[24] A. M. Gilbertson, M. Fearn, J. H. Jefferson, B. N. Murdin, P. D. Buckle, and L. F. Cohen, Phys. Rev. B **77**, 165335 (2008).

[25] M. Akabori, T. Sunouchi, T. Kakegawa, T. Sato, T.-k. Suzuki, and S. Yamada, Physica E **34**, 413 (2006).

[26] F. Herzog, H. Hardtdegen, T. Schäpers, D. Grundler, and M. A. Wilde, New J. Phys. **19**, 103012 (2017).

[27] N. S. Averkiev, M. M. Glazov, and S. A. Tarasenko, Solid State Commun. **133**, 543 (2005).

[28] S. A. Tarasenko and N. S. Averkiev, JETP Lett. **75**, 552 (2002).

[29] S. A. Tarasenko, Phys. Solid State **44**, 1769 (2002).

[30] W. Yang and K. Chang, Phys. Rev. B **73**, 045303 (2006).

[31] A. J. A. Beukman, F. K. de Vries, J. van Veen, R. Skolasinski, M. Wimmer, F. Qu, D. T. de Vries, B.-M. Nguyen, W. Yi, A. A. Kiselev, M. Sokolich, M. J. Manfra, F. Nichele, C. M. Marcus, and L. P. Kouwenhoven, Phys. Rev. B **96**, 241401(R) (2017).

[32] V. I. Fal'ko, Phys. Rev. B **46**, 4320 (1992).

[33] M. A. Wilde and D. Grundler, New J. Phys. **15**, 115013 (2013).

[34] G. Golub and C. F. van Loan, *Matrix Computations*, 4th ed. (The Johns Hopkins University Press, Baltimore, 2013).

[35] Here, we benchmark using a powerful laptop.

[36] J. Casanova, G. Romero, I. Lizuain, J. J. García-Ripoll, and E. Solano, Phys. Rev. Lett. **105**, 263603 (2010).

[37] D. Braak, Phys. Rev. Lett. **107**, 100401 (2011).

[38] D. R. Candido, S. I. Erlingsson, H. Gramizadeh, J. V. I. Costa, P. J. Weigele, D. M. Zumbühl, and J. C. Egues, Phys. Rev. Res. **5**, 043297 (2023).

[39] C. Wang, W. Duan, L. Glazman, and A. Alexandradinata, Phys. Rev. B **100**, 014442 (2019).

[40] M. Brack and R. Bhaduri, *Semiclassical Physics* (Addison-Wesley Publishing, New York, 1997).

[41] F. F. Fang and P. J. Stiles, Phys. Rev. **174**, 823 (1968).

[42] S. Brosig, K. Ensslin, A. G. Jansen, C. Nguyen, B. Brar, M. Thomas, and H. Kroemer, Phys. Rev. B **61**, 13045 (2000).

[43] A. T. Hatke, M. A. Zudov, L. N. Pfeiffer, and K. W. West, Phys. Rev. B **85**, 241305(R) (2012).

[44] I. A. Dmitriev, A. D. Mirlin, D. G. Polyakov, and M. A. Zudov, Rev. Mod. Phys. **84**, 1709 (2012).